RSC Advances

PAPER

View Article Online
View Journal | View Issue



Cite this: *RSC Adv.*, 2024, **14**, 8709

# Catalytic performance and mechanism study of the isomerization of 2,5-dichlorotoluene to 2,4-dichlorotoluene†

Jiang-Tao Ma,[ab] Teng-Fei Meng,[b] Zi-Yun Chen,[b] Yu-Jun Zhu,[c] Cheng Lian,[d] Peng Wang,[b] Ding-Hua Liu*[a] and Yu-Pei Zhao*[b]

This work investigates the influence of catalyst HZSM-5 on the isomerization of 2,5-dichlorotoluene (2,5-DCT) to produce 2,4-dichlorotoluene (2,4-DCT). We observe that hydrothermal treatment leads to a decrease in total acidity and Brønsted/Lewis ratio of HZSM-5 while generating new secondary pores. These characteristics result in excellent selectivity for post-hydrothermal modified HZSM-5 in the isomerization reaction from 2,5-DCT to 2,4-DCT. Under atmospheric pressure at 350 °C, unmodified HZSM-5 achieves a selectivity of 66.4% for producing 2,4-DCT, however after hydrothermal modification the selectivity increases to 78.7%. Density Functional Theory (DFT) calculations explore the thermodynamic aspects of adsorption between the HZSM-5 surface and 2,4-DCT. The kinetic perspective investigates the mechanism involving proton attack on the methyl group of 2,5-DCT followed by rearrangement leading to formation of 2,4-DCT during isomerization. The consistency between simulation and experimental results provides evidence for the feasibility of isomerizing 2,5-DCT to 2,4-DCT. This work fills the gap in the low value-added product 2,5-DCT isomer conversion, indicating its significant practical application potential and provides a valuable reference and guidelines for industrial research in this field.

Received 9th January 2024
Accepted 10th March 2024

DOI: 10.1039/d4ra00223g

rsc.li/rsc-advances



## 1 Introduction

Dichlorotoluene (DCT) comprises several isomers, including 2,6-DCT, 2,4-DCT, 2,5-DCT, 2,3-DCT, and 3,4-DCT. Of these isomers, the significance of 2,6-DCT and 2,4-DCT lies in their roles as crucial intermediates. Specifically within the pharmaceutical sector, they serve as essential raw materials for producing highly potent antibacterial drugs. Additionally, these compounds find applications in the manufacturing of bactericides, insecticides, herbicides, organic dyes, and other high-value-added products. The downstream products exhibit substantial growth potential, offering promising profit prospects in these sectors.

The prevalent industrial approach for synthesizing 2,6-DCT and 2,4-DCT is currently the chlorination method, which has been in use since 1965. In this method, chlorotoluene serves as the starting material, undergoing a reaction with homogeneous catalysts such as chlorinated metals and chlorine gas. However, this method suffers from several drawbacks, including high catalyst consumption, difficulties in product separation, equipment corrosion, and the generation of challenging acidic wastewater. These issues are inconsistent with the principles of 'green chemistry' that aim for sustainability and environmental friendliness. Most importantly, the chlorination method yields low selectivity for target compounds, with byproducts like 2,5-DCT showing a high 30% formation rate.[1]

Currently, there are no reports on the conversion of 2,5-DCT to the higher-value 2,4-DCT through isomerization. Non-homogeneous gas-phase isomerization methods are economically promising and environmentally friendly. They yield excellent catalytic results under mild conditions, eliminating the need for high-pressure hydrogen, thus offering significant possibilities for industrial applications. In non-homogeneous isomerization processes, solid acid catalysts, particularly zeolites, are commonly employed due to their abundant Lewis and Brønsted acid sites and exceptional thermal stability at elevated temperatures.

The acidity of zeolite catalysts primarily depends on the coordination state and distribution of aluminium species, including framework Al and extra-framework Al.[2] Various post-treatment methods, such as acid treatment,[3,4] alkali treatment,[5] and hydrothermal treatment,[6–8] can modify the catalyst's

[a]State Key Laboratory of Materials-Oriented Chemical Engineering, College of Chemical Engineering, Nanjing Tech University, Nanjing 210009, China
[b]School of Petrochemical Engineering, Changzhou University, Changzhou 213164, China
[c]Department of Pharmaceutical and Biomedical Engineering, Clinical College of Anhui Medical University, Hefei 230031, China
[d]School of Chemistry and Molecular Engineering, East China University of Science and Technology, Shanghai 200237, China

† Electronic supplementary information (ESI) available. See DOI: https://doi.org/10.1039/d4ra00223g

acidity. Among these techniques, hydrothermal treatment has garnered significant research attention owing to its convenience, cost-effectiveness, and substantial potential for industrial applications. Hydrothermal treatment not only modifies the acidity of the molecular sieve but also generates secondary pore structures, clears channels, reduces diffusion limitations, making it easier for reactant molecules to access active sites within the pores, adjusting product composition, and enhancing the selectivity of the target product.[9] Simultaneously, it reduces the number and strength of both Lewis and Brønsted acid sites, leading to improved catalytic efficiency in isomerization reactions.[10,11] Research in this field has indicated that hydrothermal temperature plays a crucial role in determining catalytic performance.[12] For instance, Zhang *et al.*,[13] observed a decrease in strong acid site quantity along with reduced acid strength within ZSM-5 zeolite following hydrothermal treatment. This reduction was particularly pronounced for external surface acid centers, as indicated by pyridine infrared spectrum data, leading to the suppression of by-product formation during reactions. Zhao *et al.*,[14] reported that hydrothermal treatment could effectively reduce the acidity of the zeolite. Moreover, hydrothermal treatment results in varying degrees of dealumination, as studied by Zhang *et al.*,[15] and Fu *et al.*,[8] who examined the effects of hydrothermal treatment on the structure and acidity of ZSM-5 zeolite.

HZSM-5 zeolite molecular sieve, known for its high-temperature resistance and strong acidity, has been widely applied in various processes, including catalytic cracking, catalytic reforming, and isomerization.[16–21] Previous studies have demonstrated the effective catalytic performance of HZSM-5 zeolite molecular sieves in isomerization reactions of dimethylbenzene and dichlorobenzene.[22–24] However, there is currently no report on the catalytic performance of HZSM-5 zeolite and hydrothermally modified HZSM-5 zeolite catalysts in the isomerization of 2,5-DCT.

In this study, HZSM-5 was chosen as the catalyst for the DCT isomerization reaction, marking the first presentation of the molecular sieve-catalysed conversion from 2,5-DCT to 2,4-DCT. We extensively investigated the influence of hydrothermal treatment on catalytic performance, characterizing acidity and structure through techniques such as BET, XRD, $NH_3$-TPD, and Py-IR. Density Functional Theory (DFT) calculations confirmed the thermodynamic favourability of HZSM-5-catalyzed transformation from 2,5-DCT to 2,4-DCT, revealing synergistic effects between L acid sites and B acid sites. Furthermore, reaction kinetics calculations indicated a relatively high energy barrier for the isomerization reaction, necessitating elevated temperatures.

# 2 Experimental

## 2.1 Materials

2,5-DCT (99%), chlorobenzene (99%) and ethanol (99%) were purchased from Aladdin Industrial Corporation. HZSM-5 (Si/Al ratio of 30) molecular sieve was purchased from Zibo Qichuang New Materials Corporation. High-purity nitrogen (99%) was purchased from Shangyuan Industrial Gas Corporation. All reagents were used without further purification.

## 2.2 Preparation of materials

The HZSM-5 molecular sieve was loaded into a small fixed-bed layer reactor and placed in a constant-temperature zone. Under a nitrogen atmosphere, the reactor was heated to 350 °C and maintained at this temperature for 3 hours for drying. Preheating treatment temperatures were set at 300 °C, 400 °C, and 500 °C. After temperature stabilization, water vapor was introduced at a constant flow rate using a syringe pump, with a liquid hourly space velocity (LHSV) of 1 $h^{-1}$. Water vapor treatment was conducted for 4 hours, and then the system was cooled down to room temperature under a nitrogen flow. The resulting HZSM-5 molecular sieves after hydrothermal treatment were denoted as HZ-300, HZ-400, and HZ-500.

## 2.3 Isomerization test

The schematic diagram of the reaction apparatus is shown in Fig. 1. After grinding the molecular sieve catalyst in a mortar, particles ranging from 20 to 40 mesh size are sieved and loaded into a fixed-bed reactor. Inert support components, such as wire mesh and quartz sand, are added to maintain the catalyst in the middle of the furnace tube. Nitrogen gas is used as the carrier gas to sweep the furnace tube, and the temperature is set. Once the temperature stabilizes, the constant-flow feed pump is opened to transport the raw materials into the preheating furnace. The vaporized raw materials are introduced into the catalytic bed with $N_2$. After the reaction stabilizes, the products are collected through condensation and analysed using gas chromatography.

# 3 Results and discussion

## 3.1 Catalyst characterization

X-ray diffraction analysis in Fig. 2a revealed that HZSM-5 subjected to hydrothermal treatment exhibited no peak shifts, and the corresponding XRD pattern matched that of the untreated sample. This observation indicates that hydrothermal treatment

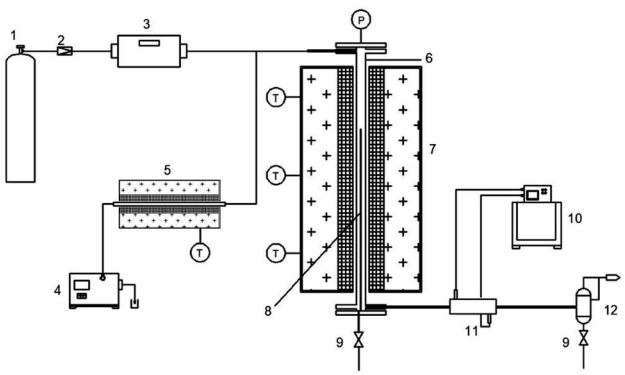


Fig. 1 Experimental equipment for 2,5-dichlorotoluene to 2,4-dichlorotoluene reaction. 1-Nitrogen cylinder, 2-pressure reducing valve, 3-mass flow meter, 4-constant flow feed pump, 5-vaporization preheating furnace, 6-reactor, 7-heating furnace, 8-thermocouple, 9-two-way ball valve, 10-low temperature thermostatic water tank, 11-condensate tube, 12-collection jar.

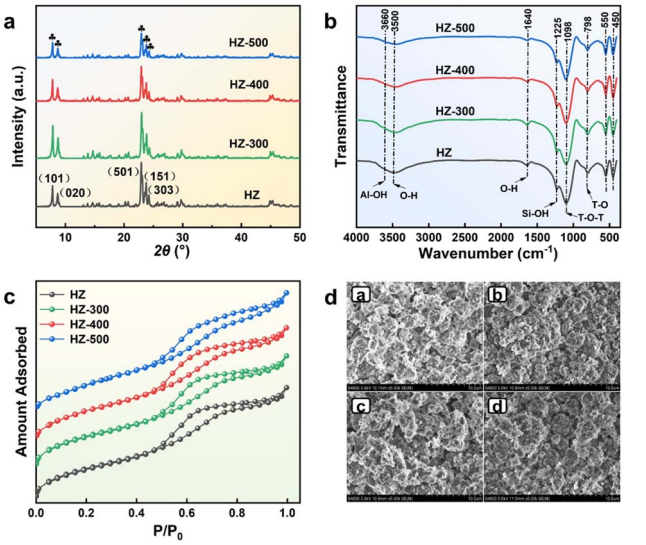


Fig. 2 (a) XRD patterns of the parent and steamed HZSM-5 zeolites. (b) FT-IR patterns of parent and steamed HZSM-5 zeolites. (c) $N_2$ adsorption–desorption isotherms of parent and steamed HZSM-5 zeolites. (d) Surface morphology of parent and steamed HZSM-5 zeolites based on SEM. (a) HZSM-5, (b) 300 °C of steaming, (c) 400 °C of steaming, (d) 500 °C of steaming.

does not induce changes in the framework structure.[25] All catalysts displayed characteristic diffraction peaks associated with the MFI-type zeolite, demonstrating the excellent hydrothermal stability of HZSM-5 molecular sieves. The primary characteristic diffraction peaks were concentrated at 8.18° (101), 9.07° (020), 23.3° (501), 24.1° (151), and 24.6° (303).[26]

The impact of hydrothermal temperature on the crystal phase structure of HZSM-5 molecular sieves was examined using FTIR spectroscopy, as shown in Fig. 2b. All catalysts exhibited broad bands centered at 3500 $cm^{-1}$ and 1640 $cm^{-1}$, corresponding to the symmetric stretching and bending vibrations of O–H bonds. Absorption peaks at 550 $cm^{-1}$ and 450 $cm^{-1}$ were associated with the stretching vibrations of double-five-membered rings in the MFI framework structure and the bending vibrations of T–O–T (T = Si or Al) units.[27] The absorption peaks at 1098 $cm^{-1}$ and 798 $cm^{-1}$ were attributed to internal vibrations of $Si(Al)O_4$ tetrahedra.[28] The peak at 1098 $cm^{-1}$ corresponded to the anti-symmetric stretching vibration of T–O–T (T = Si or Al) bonds, while the peak at 798 $cm^{-1}$ corresponded to the symmetric stretching vibration of T–O bonds. The peak at 1225 $cm^{-1}$ was attributed to the asymmetric stretching vibration of Si–OH bonds, characteristic of ZSM-5. In the range of 3660–3610 $cm^{-1}$, the peaks were associated with Al-bound hydroxyl groups, with the peak at 3660 $cm^{-1}$ related to Al–OH groups external to the framework.[29]

The hydrothermally modified HZSM-5 catalyst exhibits $N_2$ adsorption and desorption isotherms similar to those of the unmodified HZSM-5, as shown in Fig. 2c. In the low-pressure region at $P/P_0 < 0.5$, a gradual increase in adsorption is observed, characteristic of microporous molecular sieves. In the range of $P/P_0 = 0.5$–1.0, a distinct hysteresis loop is evident, corresponding to a typical mesoporous structure.

Table 1 Surface areas and pore structure features of parent and steamed HZSM-5 zeolites

| | Surface area ($m^2$ $g^{-1}$) | | | Pore volume ($mm^3$ $g^{-1}$) | |
|---|---|---|---|---|---|
| Catalyst | $S_{BET}$ | $S_{micro}$ | $S_{external}$ | $V_{total}$ | $V_{micro}$ |
| HZ | 313 | 161 | 151 | 0.27 | 0.08 |
| HZ-300 | 310 | 152 | 157 | 0.27 | 0.08 |
| HZ-400 | 302 | 130 | 171 | 0.27 | 0.07 |
| HZ-500 | 290 | 107 | 183 | 0.27 | 0.06 |

During the hydrothermal treatment process, tetrahedrally coordinated aluminium in the molecular sieve framework undergoes hydrolysis and removal. This concurrent dealumination and structural rearrangement lead to the disruption or blockage of some micropores. These structural changes result in a reduction in the specific surface area of the HZSM-5 catalyst, accompanied by an increase in the external surface area. This trend becomes more pronounced with higher hydrothermal treatment temperatures, as indicated in Table 1. Previous research has also noted a decrease in the BET surface area of HZSM-5 catalysts after hydrothermal treatment.[30,31] The total pore volume of the HZSM-5 catalyst remains relatively unchanged after hydrothermal treatment, but the micropore volume decreases with increasing hydrothermal temperature, while mesopores show varying degrees of increase (see Table 1). SEM images also illustrate this change, as shown in Fig. 2d. This is primarily attributed to hydrothermal treatment causing the removal of some framework aluminium from the molecular sieve, creating vacancies at their positions. This results in the connection of intersecting pores, forming larger secondary pores. Appropriate treatment temperatures can serve to some extent as a pore-clearing mechanism.[32]

The alterations in acid distribution within hydrothermally modified HZSM-5 zeolites were explored through $NH_3$-TPD, as illustrated in Fig. 3a. Two ammonia desorption peaks were observed in all tested molecular sieves. The high-temperature desorption peak within the range of 400–500 °C corresponds to strong acid sites in the molecular sieve, while the low-temperature desorption peak within the range of 200–300 °C corresponds to weak acid sites. With an increase in the hydrothermal treatment temperature, the areas under both the high-temperature and low-temperature desorption peaks decrease, indicating a reduction in the quantity of strong and weak acid sites, with a particularly pronounced change in the content of strong acid sites. This reduction is attributed to the fact that the acidity of HZSM-5 molecular sieves is primarily provided by framework aluminium. During the hydrothermal treatment process, a portion of the tetrahedrally coordinated hydrolysed $Al(HO)_3$ species within the molecular sieve framework dissociates, forming aluminium species fragments. This leads to a decrease in the aluminium content within the molecular sieve framework, resulting in a reduction in both acidity and the quantity of acid sites in the catalyst.

Both weak and strong acid sites of the molecular sieve catalyst undergo alterations during the hydrothermal treatment

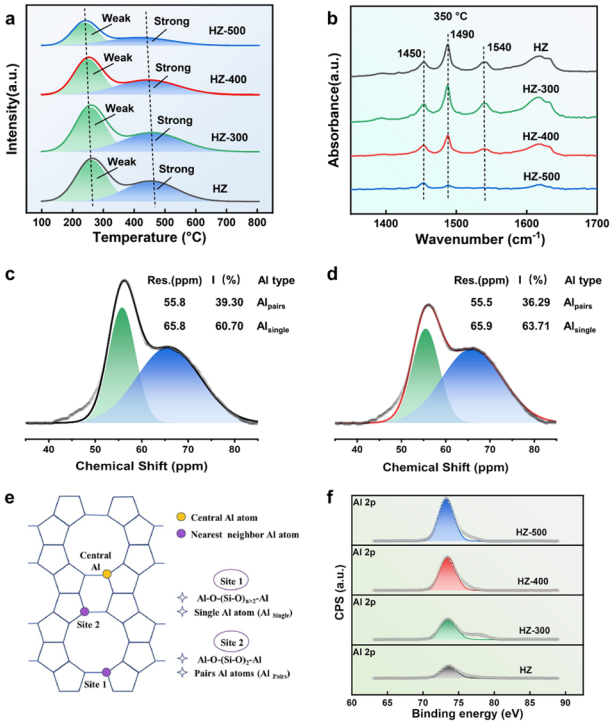


Fig. 3 (a) $NH_3$-TPD profiles of parent and steamed HZSM-5 zeolites. (b) Py-IR plots of parent and steamed HZSM-5 zeolites. (c) and (d) $^{27}Al$ SS NMR spectra of the HZ and HZ-400 samples are shown. (e) The models showing the $Al_{single}$ and $Al_{pairs}$ species.[42] (f) Al 2p XPS spectra of parent and steamed HZSM-5 zeolites.

process, as outlined in Table 2. Under the influence of hydrothermal treatment, the total acidity of the molecular sieve significantly decreases, and both desorption peaks shift towards lower temperatures. This shift indicates that, with the removal of framework aluminium, the acidity strength of HZSM-5 molecular sieve also decreases. In the case of HZ-300, undergoing low-temperature hydrothermal treatment, its acid content is not significantly different from HZSM-5, while its weak acid content is higher. This could be attributed to the purification effect of low-temperature hydrothermal treatment, which exposes small pores and acid sites on the surface. When the hydrothermal treatment temperature is raised to 500 °C, the molecular sieve undergoes substantial dealumination, with almost no observable strong acid peaks and a noticeable decrease in the weak acid peaks.

To gain deeper insights into the influence of hydrothermal treatment on the acidity of HZSM-5, pyridine adsorption infrared spectroscopy was conducted, as depicted in Fig. 3b. The acidity of HZSM-5 primarily arises from Si–OH–Al bridging hydroxyl groups and coordinatively unsaturated Al atoms, designated as B and L acid sites, respectively.[33] Surface L acid sites on the molecular sieve can be observed at 1450 $cm^{-1}$, while surface B acid sites are noticeable at 1540 $cm^{-1}$. The absorption peak at 1490 $cm^{-1}$ is attributed to the combined effect of B and L acid sites. The peak areas of B and L acid sites represent the acidity of the catalyst.[34] With increasing hydrothermal temperature, the reduction in B acid centers is more significant than that of L acid centers, as evidenced by the greater decrease in the absorption peak area of B acid sites compared to L acid sites. When the hydrothermal treatment temperature reaches 500 °C, the B acid content nearly disappears, indicating that hydrothermal treatment has a more pronounced impact on B acid centers than on L acid centers. Previous research has shown that hydrothermal treatment can reduce the quantity and strength of both B and L acid sites.[35–38] The results from the Py-IR testing align with these findings.

As the hydrothermal treatment temperature increases, the B/L ratio decreases, with both B acid and L acid content decreasing, albeit B acid content decreases at a faster rate, as indicated in Table 3. At a hydrothermal treatment temperature of 300 °C, the catalyst's B/L ratio remains relatively stable. However, at 400 °C, due to the accelerated reduction of B acid sites, the B/L ratio begins to decrease. When the temperature reaches 500 °C, the substantial reduction in B acid content results in a significant decrease in the B/L ratio.

The $^{27}Al$ SS NMR technique was employed to study the coordination of aluminium atoms, revealing the influence of hydrothermal treatment on the aluminium framework structure of HZSM-5, as illustrated in Fig. 3c and d. Both HZ and HZ-400 exhibit significant peak signals in the region of approximately 50–70 ppm, attributed to tetrahedrally coordinated framework aluminium (FAl). Comparing HZ and HZ-400, it can be observed that the peak intensity of tetrahedrally coordinated framework aluminium is notably reduced in the HZSM-5

Table 3 B/L of parent and steamed HZSM-5 zeolites

| Sample | HZ | HZ-300 | HZ-400 | HZ-500 |
|---|---|---|---|---|
| B/L | 1.84 | 1.85 | 1.50 | 0.31 |

Table 2 Desorption temperature and acid quantity of parent and steamed HZSM-5 zeolites[a]

| | $T_{peak}$ (°C) | | Acid amount (μmol $g_{cat}^{-1}$) | | |
|---|---|---|---|---|---|
| Catalyst | LT peak | HT peak | Weak acidity | Strong acidity | Total acidity |
| HZ | 261 | 468 | 369 | 258 | 627 |
| HZ-300 | 255 | 468 | 383 | 216 | 599 |
| HZ-400 | 249 | 456 | 303 | 160 | 463 |
| HZ-500 | 238 | 436 | 189 | 109 | 298 |

[a] LT peak represents low temperature desorption peak. HT peak represents high temperature desorption peak.

sample subjected to 400 °C hydrothermal treatment. This indicates that hydrothermal treatment removed a portion of the FAl species from the HZSM-5 framework.

To obtain more detailed information about the distribution of aluminium species, peak fitting was performed on the $^{27}$Al SS NMR spectra. Analysis of the asymmetric shapes of the peaks revealed the presence of two distinct resonance peaks at approximately 55.8 and 65.8 ppm, corresponding to two types of tetrahedrally coordinated framework aluminium species.[39,40] A paired aluminium atom signal ($Al_{pairs}$) at around 55.8 ppm was fitted, which is located in straight and sinusoidal pores within the zeolite. Additionally, an isolated aluminium atom signal peak ($Al_{single}$) at approximately 65.8 ppm was fitted, representing aluminium species situated at pore intersections,[41,42] Fig. 2e. Both HZ and HZ-400 samples exhibit a high content of $Al_{single}$ species. In contrast, after hydrothermal treatment, there is an increase in the number of $Al_{single}$ species and a decrease in the number of $Al_{pairs}$, Fig. 3e. During the hydrothermal process, $Al_{single}$ species exhibit greater stability compared to $Al_{pairs}$. This result aligns with the findings reported by Xu *et al.*[43]

XPS was used to quantitatively analyse the changes in surface aluminium migration, as depicted in Fig. 3f. Compared to HZSM-5, the hydrothermally treated samples exhibited increased intensity of the Al 2p peak of surface aluminium species, indicating dealumination. This change in intensity is attributed to a significant alteration in the coordination structure of aluminium after hydrothermal treatment. A portion of the tetrahedrally coordinated framework aluminium is transformed into extra-framework aluminium. This involves the substantial migration of aluminium from the framework to the surface, leading to the accumulation of surface aluminium and an increase in peak intensity. Similar results have been reported previously.[44–46]

### 3.2 Catalyst performance evaluation

**3.2.1 Influence of different hydrothermal temperatures.** Selecting untreated HZSM-5 and HZSM-5 modified at different hydrothermal temperatures, the conversion rates of reactants in the DCT isomerization reaction is shown in Fig. 4a, as well as the product selectivity in Fig. 4b, and the contents of the resulting products are detailed in Table S1.†

The hydrothermally treated HZSM-5 exhibited enhanced selectivity for 2,4-DCT. As the hydrothermal treatment temperature increased, there was a noticeable decline in the conversion rate of HZSM-5. At a modification temperature of 500 °C, the conversion rate dropped to 6.9%. This decrease was primarily attributed to the significant removal of framework aluminium within the zeolite pores, leading to a reduction in strong acid active centers and a weakening of acidity. In contrast, the selectivity for 2,4-DCT initially increased and then decreased with the rise in modification temperature. At a hydrothermal treatment temperature of 400 °C, the selectivity for 2,4-DCT peaked at 78.7%, representing an increase of nearly 13%. However, after hydrothermal treatment at 500 °C, the B acid centers nearly disappeared, causing an imbalance in the acidity ratio and a decrease in the selectivity for 2,4-DCT.

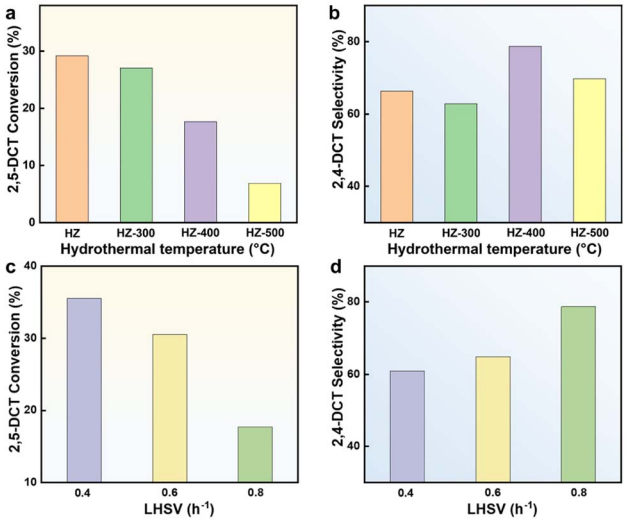


Fig. 4 (a) and (b) Catalytic performance of HZSM-5 with different hydrothermal treatment temperatures. (c) and (d) Catalytic performance of HZSM-5 isomerization of 2,5-dichlorotoluene after hydrothermal treatment at different feed velocity.

Untreated HZSM-5 exhibits a significant number of acid centers and strong acid sites on its surface, contributing to target product formation but also making it susceptible to side reactions such as aromatization. This leads to the formation of carbon deposits on the catalyst's surface, covering the strong and moderately strong acid sites and reducing isomerization efficiency. After hydrothermal modification, HZSM-5 zeolite undergoes changes in acidity; the number of strong acid sites decreases, and acidity strength diminishes, especially the reduction of external surface acid sites, effectively suppressing by-product formation.[47] Structurally, there is an increase in mesopores and mesoporous surface area, reducing diffusion resistance and enhancing the diffusion rate of reactants and products within the catalyst's pores.[48,49] This, in turn, lowers the likelihood of carbon deposition and improves product selectivity. Therefore, catalysts subjected to appropriate hydrothermal treatment exhibit suitable acid centers and pore structures, enabling higher catalytic efficiency in practical applications.

**3.2.2 Influence of different feed velocity.** Selecting HZ-400 as catalyst and keeping all other conditions constant, we varied the feed velocity to investigate the conversion rates of reactants in the DCT isomerization reaction (Fig. 4c), as well as the product selectivity (Fig. 4d). The contents of the resulting products are detailed in Table S2.†

With an increase in feed velocity, the conversion rate decreases, while the selectivity increases. Experimental results suggest that at lower feed velocities, longer reaction times facilitate thorough interaction between the feedstock and the catalyst, thereby increasing the conversion rate of 2,5-DCT. However, lower space velocities make 2,5-DCT more prone to side reactions and disproportionation, resulting in higher byproduct production and hindering improvements in product selectivity. Appropriately increasing the feed velocity can prevent the formation of other by-products, enhancing the

selectivity of the main product. Nevertheless, excessively high velocities lead to a short contact time between the feedstock 2,5-DCT and the catalyst bed, resulting in reduced conversion rates and selectivity. Data presented in the figures and tables indicate that at a feed velocity of 0.8 $h^{-1}$, the selectivity for 2,4-DCT is the highest, with minimized by-product production.

According to a report,[50] using Hβ molecular sieve as a catalyst for the isomerization of 2,5-DCT at 350 °C resulted in a conversion rate of 24.9% and a selectivity of 13.1%. In this study, HZSM-5 was chosen as the isomerization catalyst, the conversion rate of 2,5-DCT reached as high as 29.2%, while the selectivity for 2,4-DCT was 66.4%, surpassing the results reported in the literature. Furthermore, after further hydrothermal modification, HZSM-5 molecular sieve maintained a commendable conversion rate of 17.7%, with a high selectivity of 78.7% towards 2,4-DCT.

### 3.3 Simulation calculation

In order to delve deeper into the thermodynamics and kinetics of the isomerization of 2,5-DCT to 2,4-DCT, 2,6-DCT, 2,3-DCT, and 3,4-DCT on H-ZSM5 catalyst, the adsorption configurations of reactants and products were structurally optimized and subjected to single-point energy calculations using density functional theory. The initial adsorption configurations of products and reactants on the HZSM-5 surface were set as shown in Fig. S1,† and after structural optimization, the adsorption configurations of reactants and products are depicted in Fig. S2.†

Compared to their initial positions, the center of mass of DCT is located between the L acid (Al) and B acid (H), and they both shift towards Al. This observation aligns with the experimental conclusion that B acid and L acid cooperate in catalysis. Among the adsorption configurations of the four products, the average distance between 3,4-DCT and 2,4-DCT and the active sites of HZSM-5 is closer, indicating a stronger interaction between them. In contrast, the distance between 2,6-DCT and the active centers is elongated, suggesting that this product may have higher energy and is thermodynamically less favourable.

Based on the energy data along the reaction path, a reaction potential energy surface can be plotted to reveal the energy relationship between reactants and products. To further compare the thermodynamic energy differences between the four product species and the reactants, energy calculations were performed for both reactants and products before and after the reaction, using the adsorption energy calculation formula:

$$E_{ads} = E_{AB} - E_A - E_B \quad (1)$$

In the formula, $E_B$ represents the molecular energy of dichlorotoluene, $E_A$ represents the molecular sieve energy, and $E_{AB}$ represents the overall energy after adsorption.

The energies of the various structures were calculated using formula (1), and the adsorption energies for 2,5-DCT, 2,4-DCT, 2,6-DCT, 2,3-DCT, and 3,4-DCT are as follows: −0.038 eV, −0.580 eV, 0.399 eV, −0.039 eV and −0.462 eV.

Through the thermodynamic energy profile diagram in Fig. 5a, the analysis reveals that among the products, 2,4-DCT is the most thermodynamically favourable, while 2,6-DCT is thermodynamically less favourable. The electrostatic potential maps in Fig. 5b depict the charge distribution on the surfaces of the molecules of 2,5-DCT, 2,4-DCT, and 2,6-DCT. To further confirm the mechanism by which HZSM-5 enhances the isomerization of 2,5-DCT into 2,4-DCT, difference charge and Mulliken charge calculations were performed on the adsorbed 2,5-DCT configurations. The difference charge density cross-section map in Fig. 5c shows that there is a certain degree of charge transfer between HZSM-5 and the adsorbed 2,5-DCT, where HZSM-5 transfers a portion of the charge to the reactant, resulting in a charge rearrangement on the benzene ring, ultimately leading to the isomerization into 2,4-DCT. The results of the Mulliken charge analysis in Fig. 5d further indicate the presence of a chemical interaction between them. Moreover, in the presence of the catalyst, electron rearrangement takes place on the benzene ring.

In the kinetic process calculations for isomerization reactions, through transition state search, it has been discovered that the reaction pathway of HZSM-5 catalysing 2,5-DCT involves the proton attacking the C–C bond connecting the benzene ring and the adjacent methyl group within the catalyst. This proton attack induces the detachment of the methyl group, followed by charge rearrangement, with charge concentration occurring at the carbon atom adjacent to the chlorine. Subsequently, the methyl group replaces the adjacent chlorine atom. Simultaneously, the adjacent chlorine atom undergoes transposition, and the $H^+$ ion returns to the HZSM-5 catalyst. The entire process comprises two reaction steps, involving two transition states: the first one being the transposition of the methyl group to the adjacent position under the proton attack (TS1), and the second being the transposition of the chlorine

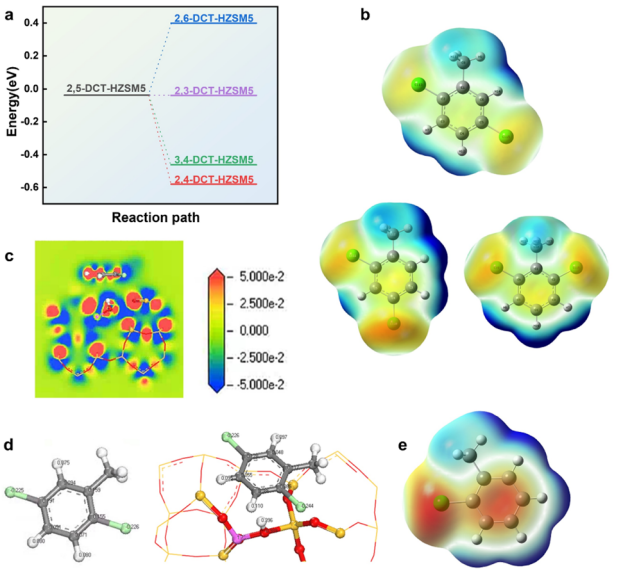


Fig. 5 (a) Thermodynamic step diagram of reactants and products, (b) difference charge density cross-section, (c) molecular Mulliken charge diagram before and after adsorption. (d) Electrostatic potential diagram, (e) thermodynamic reaction process simulation of chlorination reaction process.

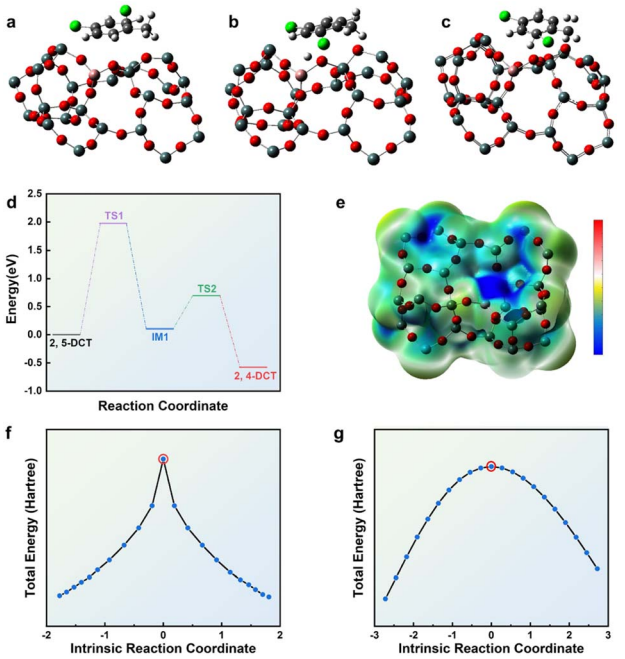


Fig. 6 (a) Transition state configuration: TS1. (b) Transition state configuration: TS2. (c) Transition state configuration: IM1. (d) Reaction path diagram. (e) Electrostatic potential diagram of selected HZSM-5 fragments. (f) IRC analysis of TS1 path process. (g) IRC analysis of TS2 path process.

atom to the adjacent position (TS2). Additionally, an intermediate species (IM1) is also involved in this process. With configurations depicted in Fig. 6a–c. The isomerization transformation is initiated by the proton attack on the methyl group within the bridging hydroxyl group in the Al–OH–Si structure.[51–54]

The pathway diagram for the DCT isomerization reaction is illustrated in Fig. 6d. The entire reaction pathway has a barrier of 1.974 eV, with the highest barrier occurring in the process where a proton attacks the methyl group to form TS1. This step has a relatively high endothermicity and serves as the rate-determining step. Effectively promoting the activation of the proton on the C–C bond of the methyl group will be a key focus for future catalyst optimization. The electrostatic potential map of the HZSM-5 fragment is presented in Fig. 6e, where the blue area represents the region with the highest electrostatic potential. This is the region where the most positive work is required to bring a positive charge from infinity, indicating that $H^+$ is released in this direction. It signifies the path for B acid to participate in the attack on 2,5-DCT. The IRC pathway analysis is depicted in Fig. 6f and g, searching for the transition state configuration from both forward and reverse directions yields only one identical structure pointing towards the product. This demonstrates the accuracy and uniqueness of the transition state search structures.

### 3.4 Apply simulation comparisons

In industrial applications, DCT production involves a one-step chlorination method of chlorotoluene, utilizing metal chlorides as catalysts. According to Zhu *et al.*,[1] chlorination with highly Lewis acidic metal chlorides favours the conversion of *ortho*-chlorotoluene to 2,6-DCT, reducing the formation of 2,4-DCT. The thermodynamic simulation of the chlorination process is illustrated in Fig. 5e. Simulation calculations suggest that in the chlorination reaction, the most electropositive position for chlorotoluene is at the 6th position, making it more susceptible to nucleophilic attack. Thermodynamically and mechanistically, this configuration favours the formation of 2,6-DCT, aligning with the observed results in industrial applications. In the studied isomerization system, employing HZSM-5 molecular sieves as catalysts enables the isomerization of 2,5-DCT into 2,4-DCT, and both the thermodynamics and kinetics of the process are consistent with experimental results.

A thorough examination of the computational outcomes underscores temperature as the pivotal factor influencing the isomerization pathway. With increasing temperature to a certain extent, 2,5-DCT can ultimately convert into 2,6-DCT. From a purely molecular perspective, independent of the catalyst, 2,4-DCT exhibits the lowest energy, but the organic mechanism tends toward 2,6-DCT. At 350 °C, the energy barrier from 2,5-DCT to 2,4-DCT can be overcome, while the barrier to 2,6-DCT is significantly higher. In the researched system, the solid acid functions within a suitable temperature range, insufficient to overcome the energy barrier. Elevating the temperature would lead to rapid catalyst deactivation due to coking. It is noteworthy that no previous study has offered an effective simulation and verification of the chlorination and isomerization directions in this system. The simulation results presented in this study align excellently with experimental findings (refer to Table S3†).

## 4 Conclusions

In this study, we present a novel approach to effectively enhance the selectivity of the primary product in original HZSM-5 by adjusting the catalyst's hydrothermal treatment temperature and reaction space velocity. Experimental results demonstrate that an appropriately chosen hydrothermal treatment temperature can modulate the acidity of the catalyst, leading to the formation of new mesopores, all conducive to the isomerization of DCT. Simultaneously, the judicious increase in space velocity is advantageous for suppressing the generation of by-products and improving the selectivity of the main product. Moreover, microscopic structural characterization reveals that $Al_{single}$ sites are more stable than $Al_{pairs}$ sites. Hydrothermal treatment selectively deals with $Al_{pairs}$ positions within the zeolite framework, triggering an increase in the selectivity of 2,4-DCT. Density Functional Theory (DFT) calculations substantiate the thermodynamic feasibility of this isomerization reaction, providing a theoretical foundation. In kinetic calculations, it is discovered that the conversion of DCT isomerization is initiated by a proton attack on the methyl group in the Al–OH–Si structure. A comparison of chloride reactions and transposition reactions, both in simulation and experimental results, confirms consistency, affirming that in the isomerization reaction, using a molecular sieve as a catalyst at a specific

temperature, 2,5-DCT can be transformed into 2,4-DCT. Subsequently, resourceful reuse of waste can be achieved through cyclic reactions. This work provides new insights and explorations into the industrial application of the isomerization reaction of 2,5-DCT.

## Author contributions

Jiang-Tao Ma: investigation, data curation, writing – original draft, writing – review & editing-supporting. Teng-Fei Meng and Zi-Yun Chen: investigation, performed some experiments and tests. Yu-Jun Zhu and Lian Cheng: providing simulations and calculations. Peng Wang: guided the characterization analysis of samples. Ding-Hua Liu and Yu-Pei Zhao: funding acquisition, project administration, supervision, writing – review & editing.

## Conflicts of interest

The authors declare that they have no conflict of interest.

## Acknowledgements

The research received support from various funding sources, including National Natural Science Foundation of China (No. 22072007), Jiangsu Province Project of Industry-University-Research Cooperation (No. BY20221141), Zhenjiang Key Research and Development Program (Industry Foresight and Common Key Technologies, No. CQ2022006), Changzhou Applied Basic Research Program (No. CJ20220189), and the Jiangsu Graduate Workstation. These funding agencies played a crucial role in facilitating and advancing the research endeavours outlined in the study.

## References

1 X. Zhu, Y. Fu, H. Yin, A. Wang and X. Hou, *React. Kinet., Mech. Catal.*, 2016, **118**, 523–536.
2 M. Ravi, V. L. Sushkevich and J. A. van Bokhoven, *Nat. Mater.*, 2020, **19**, 1047–1056.
3 B. P. S. Santos, D. Almeida, M. D. F. V. Marques and C. A. Henriques, *Fuel*, 2018, **215**, 515–521.
4 R. Feng, B. Liu, P. Zhou, X. Yan, X. Hu, M. Zhou and Z. Yan, *Appl. Catal., A*, 2022, **629**, 118422.
5 J. Li, M. Liu, X. Guo, S. Xu, Y. Wei, Z. Liu and C. Song, *ACS Appl. Mater. Interfaces*, 2017, **9**, 26096–26106.
6 Z. Wei, L. Chen, Q. Cao, Z. Wen, Z. Zhou, Y. Xu and X. Zhu, *Fuel Process. Technol.*, 2017, **162**, 66–77.
7 A. P. Hawkins, A. Zachariou, S. F. Parker, P. Collier, N. Barrow, I. P. Silverwood, R. F. Howe and D. Lennon, *Rsc Adv.*, 2020, **10**, 23136–23147.
8 T. Fu, C. Cao, L. Zhang, L. Zhang, Q. Ma, Z. Xu, R. Wang, H. Li and Z. Li, *Ind. Eng. Chem. Res.*, 2023, **62**, 1865–1876.
9 S. Mitchell, M. Boltz, J. Liu and J. Pérez-Ramírez, *Catal. Sci. Technol.*, 2017, **7**, 64–74.
10 L. Sun, X. Guo, M. Liu and X. Wang, *Appl. Catal., A*, 2009, **355**, 184–191.
11 Y. Wang, K. Fu, H. Huang, C. Shan, Y. Zheng, R. Han and Q. Liu, *Catal. Sci. Technol.*, 2023, **13**, 3221–3225.
12 X. Zhao, X. Guo and X. Wang, *Fuel Process. Technol.*, 2007, **88**, 237–241.
13 R. Zhang, Y. Ju, P. Wu, J. Chen, Z. Lv, Y. Zhang, S. Song, Z. Zhang, C. Ma, R. Zhang and Z. Wu, *Catal. Today*, 2022, **405–406**, 57–65.
14 L. Zhao, H. Wang, M. Liu, X. Guo, X. Wang, C. Song and H. Liu, *Chem. Eng. Sci.*, 2008, **63**, 5298–5303.
15 S. Zhang, Y. Gong, L. Zhang, Y. Liu, T. Dou, J. Xu and F. Deng, *Fuel Process. Technol.*, 2015, **129**, 130–138.
16 V. Van Speybroeck, K. Hemelsoet, L. Joos, M. Waroquier, R. G. Bell and C. R. A. Catlow, *Chem. Soc. Rev.*, 2015, **44**, 7044–7111.
17 Y. Wang, X. Zhang, G. Zhan, M. Wang, W. Li and J. Cao, *Mol. Catal.*, 2023, **540**, 113044.
18 R. Jin, H. Hu, J. Wang, Z. Zhang, C. Dai and X. Ma, *New J. Chem.*, 2022, **46**, 8443–8450.
19 Y. Wang, H. An, H. Ma, X. Zhang, G. Kang and J. Cao, *Adv. Powder Technol.*, 2021, **32**, 1869–1880.
20 D. Ma, Y. Shu, W. Zhang, X. Han, Y. Xu and X. Bao, *Angew. Chem., Int. Ed.*, 2000, **39**, 2928–2931.
21 Y. Song, L. Zhang, G. Li, Y. Shang, X. Zhao, T. Ma, L. Zhang, Y. Zhai, Y. Gong, J. Xu and F. Deng, *Fuel Process. Technol.*, 2017, **168**, 105–115.
22 H. Rajaei, F. Esmaeilzadeh and D. Mowla, *Catal. Lett.*, 2022, **152**, 139–150.
23 S. H. Farahani, C. Falamaki and S. M. Alavi, *Int. J. Chem. Kinet.*, 2020, **52**, 368–377.
24 D. Kaucky, F. Fajula, P. Moreau and A. Finiels, *Appl. Catal., A*, 2003, **243**, 301–307.
25 D. P. Serrano, R. A. García, M. Linares and B. Gil, *Catal. Today*, 2012, **179**, 91–101.
26 H. Li, S. He, K. Ma, Q. Wu, Q. Jiao and K. Sun, *Appl. Catal., A*, 2013, **450**, 152–159.
27 Y. Zhao, B. Shen and H. Sun, *Ind. Eng. Chem. Res.*, 2016, **55**, 6475–6480.
28 E. M. Flanigen, H. Khatami and H. A. Szymanski, *Advances in Chemistry*, American Chemical Society, Washington, DC, 1974.
29 U. Olsbye, S. Svelle, M. Bjørgen, P. Beato, T. V. W. Janssens, F. Joensen, S. Bordiga and K. P. Lillerud, *Angew. Chem., Int. Ed.*, 2012, **51**, 5810–5831.
30 O. D. Mante, F. A. Agblevor, S. T. Oyama and R. McClung, *Appl. Catal., A*, 2012, **445–446**, 312–320.
31 F. L. Mendes, V. L. Ximenes, M. B. B. de Almeida, D. A. Azevedo, N. S. Tessarolo and A. de Rezende Pinho, *J. Anal. Appl. Pyrolysis*, 2016, **122**, 395–404.
32 J. C. Groen, J. A. Moulijn and J. Pérez-Ramírez, *Microporous Mesoporous Mater.*, 2005, **87**, 153–161.
33 D. X. Martínez-Vargas, L. Sandoval-Rangel, O. Campuzano-Calderon, M. Romero-Flores, F. J. Lozano, K. D. P. Nigam, A. Mendoza and A. Montesinos-Castellanos, *Ind. Eng. Chem. Res.*, 2019, **58**, 15872–15901.
34 S. M. T. Almutairi, B. Mezari, E. A. Pidko, P. C. M. M. Magusin and E. J. M. Hensen, *J. Catal.*, 2013, **307**, 194–203.

35 H. Yang, R. J. Coolman, P. Karanjkar, H. Wang, Z. Xu, H. Chen, T. J. Moutziaris and G. W. Huber, *Green Chem.*, 2015, **17**, 2912–2923.
36 L. R. Aramburo, S. Teketel, S. Svelle, S. R. Bare, B. Arstad, H. W. Zandbergen, U. Olsbye, F. M. F. de Groot and B. M. Weckhuysen, *J. Catal.*, 2013, **307**, 185–193.
37 B. Song, Y. Li, G. Cao, Z. Sun and X. Han, *Front. Chem. Sci. Eng.*, 2017, **11**, 564–574.
38 A. A. Gusev, A. C. Psarras, K. S. Triantafyllidis, A. A. Lappas and P. A. Diddams, *Molecules*, 2017, **22**, 1784.
39 A. Omegna, J. A. V. Bakhoven, R. Prins, M. Watanabe and J. R. Lakowicz, *J. Phys. Chem. B*, 2003, **107**, 8854.
40 N. Xue, A. Vjunov, S. Schallmoser, J. L. Fulton, M. Sanchez-Sanchez, J. Z. Hu, D. Mei and J. A. Lercher, *J. Catal.*, 2018, **365**, 359–366.
41 T. Fu, C. Cao, L. Zhang, L. Zhang, Q. Ma, Z. Xu, R. Wang, H. Li and Z. Li, *Ind. Eng. Chem. Res.*, 2023, **62**, 1865–1876.
42 M. Ibáñez, E. Epelde, A. T. Aguayo, A. G. Gayubo, J. Bilbao and P. Castaño, *Appl. Catal., A*, 2017, **543**, 1–9.
43 Z. Xu, T. Fu, Y. Han, Z. Li and G. Zhan, *Fuel*, 2023, **349**, 128671.
44 K. Chen, J. Zhao, A. Li, G. Li, Q. Zhang, T. Xia, H. Zhao, X. Zhu, H. Liu, X. Gao, C. Xu and B. Shen, *Microporous Mesoporous Mater.*, 2022, **338**, 111969.
45 A. R. Maag, G. A. Tompsett, J. Tam, C. A. Ang, G. Azimi, A. D. Carl, X. Huang, L. J. Smith, R. L. Grimm, J. Q. Bond and M. T. Timko, *Phys. Chem. Chem. Phys.*, 2019, **21**, 17880–17892.
46 J. Datka, S. Marschmeyer, T. Neubauer, J. Meusinger, H. Papp, F.-W. Schütze and I. Szpyt, *J. Phys. Chem. B*, 1996, **100**, 14451–14456.
47 Q. Sheng, K. Ling, Z. Li and L. Zhao, *Fuel Process. Technol.*, 2013, **110**, 73–78.
48 P. Voogd and H. Van Bekkum, *Appl. Catal.*, 1990, **59**, 311–331.
49 K. Rajagopalan, A. W. Peters and G. C. Edwards, *Appl. Catal.*, 1986, **23**, 69–80.
50 C. Zhai, H. Yin, J. Li, A. Wang, L. Shen and J. Hu, *React. Kinet., Mech. Catal.*, 2017, **122**, 369–384.
51 F. Richard, T. Boita, M. Moreau, C. Bachmann and G. Pérot, *J. Mol. Catal. A: Chem.*, 2007, **273**, 48–54.
52 T. Demuth, P. Raybaud, S. Lacombe and H. Toulhoat, *J. Catal.*, 2003, **222**, 323–337.
53 M. Guisnet, N. S. Gnep and S. Morin, *Microporous Mesoporous Mater.*, 2000, **35–36**, 47–59.
54 H. Tian, S. Liu and Q. Liu, *Rsc Adv.*, 2022, **12**, 24654–24669.